Research Report

The Influence of He Ion Irradiation on the Mechanical Properties of (Hf-Ta-Ti-V-Zr)-Nitride/-Carbide/-Boride Thin Films

conducted in the frame of a Marshall Plan Scholarship, at University of California, Berkeley, Department of Nuclear Engineering,

by

Dipl. Ing. Thomas Astecker, BSc

Looh 29, 4861 Aurach am Hongar, Austria

under the supervision of

Senior Scientist Dipl.-Ing. Dr.techn. Alexander Kirnbauer,

Prof. Dipl.-Ing. Dr. mont Peter Hosemann

and

Univ.-Prof. Dipl.-Ing. Dr. mont. Paul Heinz Mayrhofer

Vienna, July 2024

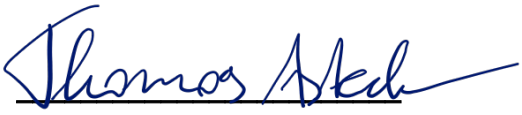

Signature

Acknowledgements

My sincere gratitude goes to Dr. Alexander Kirnbauer for sparking this incredible journey. His initial suggestion, unwavering motivation throughout the application process, and guidance during my stay at Berkeley were invaluable. I also extend my deepest thanks to Prof. Dr. Paul Heinz Mayrhofer for his immediate support, providing essential resources, and sharing his expertise.

My Berkeley experience wouldn't have been the same without Prof. Dr. Peter Hosemann and the entire Nuclear Materials Research Group. Their warmth, friendliness, and knowledge shared throughout my research project were instrumental to its success.

To my family and friends, thank you for your unwavering support throughout this enriching experience. Your understanding and encouragement allowed me to pursue this opportunity abroad.

Lastly, I am incredibly grateful to the Marshall Plan Foundation for making this research stay possible and I thank the TU Wien International Office for their guidance.

This unforgettable time in Berkeley will forever hold a special place in my memories.

Table of Contents

Abstract I
List of figures III
List of tables V
List of Abbreviations and Symbols V
1 Introduction 1
1.1 Material challenges for plasma facing components in nuclear fusion 1
1.2 High-entropy alloys 2
1.3 Thin films 3
1.4 Helium in solids 3
1.5 Possible reasons for different responses to He implantation 4
2 Experimental 6
2.1 Sample synthesis 6
2.2 X-ray diffraction 7
2.3 Energy-dispersive X-ray spectroscopy 7
2.4 Helium implantation 8
2.5 Atomic force microscopy 9
2.6 Nanoindentation 9
2.7 Electron microscopy 10
2.8 Pillar compression 10
2.9 Pre-notched micro-cantilevers 13
3 Results and Discussion 15
3.1 X-ray diffraction 15
3.2 Chemical composition 16
3.3 Fracture cross-sections 17
3.4 Helium implantation/swelling 17
3.5 Nanoindentation 20
3.6 TEM cross-sections 22
3.7 Pillar compression testing 27
3.8 Micro-cantilever fracture testing 31
4 Summary and Conclusion 32
5 List of references 33

Abstract

Fossil fuels are finite resources, and their continued use contributes to environmental damage, leading to one the most substantial challenges for modern civilization. Nuclear fusion offers a long-term solution, potentially providing a stable and abundant energy supply for generations to come. Recent technological advancements are making fusion a more realistic possibility. Research is continuously improving our understanding of plasma physics and developing more efficient methods for achieving and sustaining fusion reactions. One of the bottlenecks on the way to fusion energy is the search for materials capable of withstanding the harsh environments within such reactors.

High-entropy ceramic thin films composed of refractory elements (Hf, Ta, Ti, V, Zr) are promising candidates for first wall materials in nuclear fusion reactors due to their exceptional properties. However, it must be understood how they respond to irradiation, as this is a key concern for their long-term performance in a nuclear fusion power plant.

This study investigates the influence of He ion irradiation on the mechanical properties of (Hf-Ta-Ti-V-Zr)-nitride, -carbide, and -boride thin films and thus provides valuable insights into the suitability of high-entropy materials for fusion reactor applications. The samples were fabricated using magnetron sputtering and subsequently irradiated with He ions at fluences between 5e16 and 1.2e18 ions/cm^2 within a He ion microscope. Despite their strong elemental similarity, the films showed distinct behaviors upon the identical treatments. We found that the carbide sample shows volumetric swelling values (ΔV = 15.12±0.75 % at 5e17 ions/cm^2) very similar to W, which is the material currently in the focus of research for first wall fusion. The nitride and boride however show considerably less swelling (ΔV = 10.72±1.20 % and 11.71±0.47 % at 5e17 ions/cm^2). The hardness and elastic modulus of our nitride, carbide and boride films in the unirradiated state were 26.9±1.3 and 372±14 GPa, 32.4±1.5 and 409±13 GPa, 38.9±0.7 and 435±6 GPa. The same trend as in the swelling can also be found again in the mechanical properties, where the carbide showed the largest relative degradation (ΔH = -38.2±7.5 % compared to -20.1±1.7 % and -27.5±6.2 % for the boride and nitride at 5e17 ions/cm^2) upon irradiation. The results of pillar compression tests confirmed this tendency as well. Calculations based on a micromechanics model that estimates the modulus decrease depending on the microporosity agreed well with the measured values. Only the carbide was an outlier as its experimental values were lower than the calculations would suggest. It has been

proposed in previous studies that the main mechanism for void growth in higher hardness materials is the inter-cracking of the He microbubbles. We were able to confirm this for our films too by STEM imaging of the microstructures after irradiation. There we were also able to show the weakening effect of the He on the grain boundaries. Micro-cantilever fracture experiments revealed that the carbide film has the lowest fracture toughness of the three samples leading us to the conclusion that the excessive drop in mechanical properties is connected to the easier inter-cracking of the He bubbles upon loading.

List of figures

Fig. 1 Example EDS spectrum of a HfTaTiVZr carbide. 8
Fig. 2 Pillars prepared on sample fracture edge by FIB-milling. 11
Fig. 3 Schematic illustration of our pillar implantation and testing setup. 11
Fig. 4 Exemplary before and after SEM images of an in-situ compression test of our HfTaTiVZr boride thin film. 12
Fig. 5 Final dimensions of our pre-notched micro-cantilever prepared by FIB-milling on sample fracture edge. 13
Fig. 6 In-situ testing procedure of our micro-cantilevers inside a SEM system using a FemtoTools nanoindenter equipped with a Berkovich tip. 14
Fig. 7 X-ray diffraction patterns of our HfTaTiVZr nitride (bottom), carbide (center) and boride (top) thin films deposited with a substrate temperature of 450 °C. Reference data for a cubic phase with a lattice constant of 4.409 Å (diamonds), a tetragonal phase with a lattice constants of a=4.375 Å and c=4.457 Å (diamonds with center dot), a cubic phase with a lattice constant of 4.501 Å (cubes), a hexagonal phase with a lattice constants of a=3.115 Å and c=3.332 Å (hexagons) as well as the sapphire (Al_2O_3) substrate (crosses) is indicated. 15
Fig. 8 Chemical composition of our HfTaTiVZr boride (hexagons), nitride (diamonds) and carbide (cubes) thin films, obtained by SEM-EDS. 16
Fig. 9 Fracture cross-sections of our HfTaTiVZr (a) nitride, (b) carbide and (c) boride thin films. The white bar in the lower right corner of each image represents a length of 2 µm while the bar on the left side marks the interface between film and substrate. 17
Fig. 10 Results of SRIM simulations for 25 keV He ion implantation to a dose of 5e17 ions/cm² 18
Fig. 11 Roughness values (Rz; Ra) of our HfTaTiVZr nitrides (diamonds), carbides (cubes) and borides (hexagons). 18
Fig. 12 Percentage of volumetric swelling of our HfTaTiVZr carbides (cubes), borides (hexagons) and nitrides (diamonds) as well as Ti nitride (pentagons) depending on the implanted He dose, measured by AFM. A linear interpolation of the tungsten swelling value (taken from [15]) is displayed by the dash-dotted line. 19
Fig. 13 3D contour plots of our HfTaTiVZr borides after He implantation, obtained by AFM. 19

Fig. 14 Different modes of blistering observed on our HfTaTiVZr (a) nitride, (b) carbide, and (c) boride thin films. Please note that the He dose and the stage of blistering is not the same on all samples. ..... **Fehler! Textmarke nicht definiert.**
Fig. 15 Hardness and elastic modulus of our HfTaTiVZr boride, carbide and nitride thin films in the as deposited state as well as irradiated with different doses of He (left – H,E over He dose; right – H,E over ΔV). 21
Fig. 16 Elastic modulus of our HfTaTiVZr boride, carbide and nitride thin films in the as deposited state as well as irradiated with different doses of He measured by nanoindentation as well as calculated from the volumetric swelling by a micromechanics model proposed in [28] 22
Fig. 17 STEM dark field images of the microstructure of our HfTaTiVZr (a) boride, (b) carbide and (c) nitride thin films upon 25 keV He implantation at dose of 5e17 ions/cm². 23
Fig. 18 Comparison of microstructure overlayed with SRIM calculations (not accounted for swelling) of our HfTaTiVZr (a) nitride (bright filed), (b) carbide (dark field) and (c) boride (bright field) thin films upon 25keV He implantation at dose of 5e17 ions/cm². 24
Fig. 19 STEM cross-section images of our HfTaTiVZr nitride thin film implanted with 25 keV He ions to a dose of 5e17 ions/cm². 24
Fig. 20 STEM cross-section images of our HfTaTiVZr carbide thin film implanted with 25 keV He ions to a dose of (a) 1.2e18 and (b) 5e17 ions/cm². 25
Fig. 21 STEM cross-section images of our HfTaTiVZr boride thin film implanted with 25 keV He ions to a dose of (a), (b) 8e17 and (c) 5e17 ions/cm². 25
Fig. 22 SAED patterns of our HfTaTiVZr (a) nitride, (b) carbide and (c) boride thin film in the as deposited as well as He ion irradiated state. 26
Fig. 23 Characteristic load-displacement curves of our as deposited (solid lines) as well as He irradiated (dash-dotted lines) HfTaTiVZr boride, carbide and nitride thin film pillar compression tests. 27
Fig. 24 Results of SRIM simulations for 25 keV He ion implantation under 45° stage tilt from two sides to a dose of 3e17 ions/cm². 28
Fig. 25 SEM images of our pillars recorded after testing. The two main failure modes observed over all tested pillars were (a) shearing and (b) cracking. 28
Fig. 26 Critical strain and stress values of our HfTaTiVZr boride, carbide and nitride thin film pillar compression tests obtained from the corresponding load-displacement curves. 29
Fig. 27 Elastic modulus values of our HfTaTiVZr boride, carbide and nitride thin film pillar compression tests curves in comparison to the indentation moduli. 30

Fig. 28 Fracture toughness (left axis) as well as change of hardness upon He implantation at 5e17 ions/cm² (right axis) of our HfTaTiVZr carbide, nitride and boride thin films. 31

List of tables

Tab. 1 Chemical composition of our HfTaTiVZr boride (hexagons), nitride (diamonds) and carbide (cubes) thin films, obtained by SEM-EDS. 16

List of Abbreviations and Symbols

AFM .....*atomic force microscopy*
bcc.....*body-centered cubic*
CSM.....*continous stiffness measurement*
DC.....*direct current*
dpa.....*displacements per atom*
fcc.....*face-centered cubic*
FIB-SEM.....*focused ion beam scanning electron microscope*
hcp .....*hexagonal close-packed*
HEA.....*high-entropy alloy*
HIM.....*helium ion microscopy*
PVD.....*physical vapour deposition*
SRIM.....*Stopping Range of Ions in Matter*
TEM .....*transmission electron microscopy*
XRD.....*X-Ray diffraction*

1 Introduction

The production of clean energy is one of the pivotal problems of our current society, as the negative effects of climate change can already be observed all over the planet, and the demand for electric energy is even expected to increase drastically soon due to computing needs for artificial intelligence or transportation, only to mention two major examples. Next to solar power, wind energy and hydro energy, which all come with their own specific challenges concerning applicability and scalability, one must not forget about nuclear power generation. Nuclear fission is an already well developed and available technology but has somewhat fallen from grace in western culture due to numerous major accidents in the past and the general risks involved. Apart from that, fusion based reactors could play a role in satisfying the strongly increasing demand for energy reliably, and in a clean way, as it is superior compared to fission concerning waste production, risk of contaminating the environment, potential use as a nuclear weapon and even fuel availability. Unfortunately, many challenges still must be overcome to make fusion energy feasible. One of the essential limiting factors in the development of novel fusion and even fission reactors is the availability of materials able to withstand the harsh environments present. Especially materials of the plasma facing components need to be selected carefully to restrict the surface degradation through irradiation by high energy helium (He), hydrogen (H) isotopes and neutrons along with high thermal loads which could eventually lead to a critical failure [1].

1.1 Material challenges for plasma facing components in nuclear fusion

A first wall material in a nuclear fusion reactor must face a multitude of challenges due to the harsh circumstances it lives in [1]. The most promising fuel for nuclear fusion is a reaction based on the light hydrogen isotopes deuterium and tritium. One of the main concerns for research nowadays are the high energetic neutrons and alpha particles, released by this reaction, which bombard the first wall material leading to disruptions in its crystal lattice structure. Implantation of these species can also lead to a degradation in mechanical properties and especially ductility accompanied by swelling of the components [2].

A nuclear fusion plasma operates at extremely high temperatures accompanied with temperature peaks. A large portion of this heat load needs to be absorbed and transported off by the first wall material. This means it needs to be able to withstand high temperatures without degradation and also a high temperature gradient across the material causing thermal stresses [1].

Lastly, a first wall material needs to be chemically compatible with the coolant which could be either liquid He or lithium (Li).

1.2 High-entropy alloys

Concerning the research towards high-performance materials the high-entropy concept represents a revolutionary invention of the past decades. Initiated by Brian Cantor in 1981 [3, 4] and complemented by Yeh et al. form 2004 on [5], such high-entropy alloys (HEAs) have already proven to be able to outperform the classical alloys in many ways. The underlying principle is basically the combination of a high number of elements in similar amounts to enhance the entropy of mixing, which is then said to stabilize a solid solution phase. Yeh et al. proposed four effects as decisive for the special properties of HEAs, being lattice distortion, sluggish diffusion, the entropy stabilization, and the cocktail effect [6].

In more recent years, the concept has been complemented with non-metallic components to high-entropy ceramics. In such, to be precise, the high-entropy effect is only in force for the metallic sublattice while the non-metallic sublattice remains ordered. Because of this a group of researchers at TU Wien has invented the term high-entropy metal-sublattice borides, carbides, nitrides, or oxides [7]. This designation will also be used within this work.

HEAs comprise promising candidates for nuclear materials as the traditional engineering alloys often fall short in such applications. Especially, in the case of nuclear fusion where high temperatures are combined with a high flux of neutrons, He and H, strong magnetic fields, and corrosion from coolants. Until today only limited research has been done on HEAs and their ceramic variants in nuclear environments but the consensus of the already published studies is that they indeed can have special resistance to irradiation [8, 9, 10].

1.3 Thin films

Thin films, microscopic layers of material deposited on a substrate, hold immense potential across various industries. Their applications range from anti-reflective coatings in solar panels for improved efficiency to wear-resistant layers on cutting tools that extend their lifespan.

In the realm of nuclear energy, thin films play a crucial role in enhancing reactor performance and safety. They can be used as protective coatings for critical components, mitigating wear and tear from harsh operating environments. This not only extends the lifetime of these components but also reduces the frequency of replacements, lowering waste generation. Overall, thin films offer a promising approach for resource-conscious advancements in the nuclear energy sector.

Within this work, physical vapor deposition (PVD), or more precise magnetron sputtering, was used for the synthesis of our samples. It is a highly controlled technique for depositing thin films of various materials onto a substrate. It offers exceptional precision and allows for the creation of uniform, high-quality coatings with thicknesses ranging from a few nanometers to several micrometers. In sputtering, a target material is bombarded with energetic particles (usually inert gas ions). This bombardment dislodges atoms from the target, causing them to travel in a straight line until they collide with and adhere to the object being coated.

1.4 Helium in solids

He is a noble gas with unique properties that present challenges for materials used in fusion reactors. These challenges stem from the specific electronic configuration of a He atom. With two protons, two neutrons, and two electrons confined to the 1s orbital, He possesses a complete outer shell. This complete shell eliminates the tendency to share electrons with other atoms, preventing the formation of strong covalent or ionic bonds commonly observed in other gases. The only binding force present is the weak Van der Waals interaction, which is insufficient to overcome the He atom's zero-point energy at normal pressure. Only under extreme pressures are He atoms forced close enough for the formation of solid He.

Due to this limited bonding capability, He exhibits very low solubility in most solids. This presents a significant problem for materials deployed in environments with high-energy He ions, such as fusion reactors. He's small size allows it to easily penetrate the

crystal lattice of a material, accumulating and forming voids. These voids weaken interatomic bonds, leading to a degradation of material strength and ductility. Additionally, the internal pressure buildup within these voids causes volumetric swelling and generates stress concentrations, increasing the risk of crack formation. Ultimately, this sequence of events can culminate in catastrophic material failure. Therefore, a thorough understanding of He interaction with potential fusion reactor materials is crucial for their successful implementation.

1.5 Possible reasons for different responses to He implantation

The behavior of a material upon He implantation is based on a complex interplay between crystal structure, microstructure, atomic bonding, mechanical properties and chemical interactions.

The way in which the atoms are ordered and the presence of defects within the lattice influences how the He is able to diffuse and accumulate within a material. The most prevalent crystal structures for metals are body-centered cubic (bcc), face-centered cubic (fcc) and hexagonal close-packed (hcp). Assuming atoms (or spheres) of equal size, fcc and hcp achieve the highest possible packing density of 74 % while the packing density of bcc is with 68 % slightly lower. This has been proposed before as a reason why a bcc lattice would be more radiation resistant compared to fcc [11] lattices as it would theoretically mean that bcc lattices are able to accommodate more He at similar swelling values and enable for easier diffusion. Generally, fcc lattices are known to be the most ductile of the three crystal systems due to their dense packing and availability of slip systems, while the deformation of bcc materials is more limited and dependent on temperature. The deformation of the hcp lattice is generally complex as it possesses the least number of slip systems and the activation of those is considerably dependent on the stress direction. These considerations concerning deformation also play into the strain hardening rates which is higher if more dislocations are created. In this work we investigate transition metal ceramics which are high hardness and brittle by nature so the deformation through slip at room temperature is expected to be very limited. The main deformation mechanism here is likely the formation of microcracks or grain boundary sliding.

The orientation of a crystal lattice can also have an effect as ion channeling can occur in certain open directions, meaning that the affected material depth is larger as the ions travel further and thus swelling would be less at the same dose [12].

The size of the grains and thus the number of grain boundaries influences the response of a material upon He implantation. Grain boundaries act as trapping sites for He, respectively nucleation sites for He bubbles. If the grains are small this also means that the diffusion path for He is shorter to reach such a trapping site. It has been shown by El-Atwani et al. [13] for W that below a grain size threshold of 35 nm, the grain boundaries act as sinks to remove vacancies and thus effectively reduce swelling respectively radiation damage.

He trapping sites can also be other defects in a material such as dislocations, vacancies, precipitates, and phase boundaries.

The mechanical properties should theoretically affect the tendency of a material to swell upon He implantation. A higher modulus material should deform less at the same pressure buildup within its lattice compared to a lower modulus one. Also, a higher strength material will be able to resist the internal pressure buildup form the He bubbles longer before catastrophic failure. It has been proposed [14] and shown [15] that the mechanism for blister formation and growth upon He implantation is the formation of nanocracks in between the bubbles thus forming a larger cavity. With this in mind, the fracture toughness of a material should also have an influence on the blister formation.

This work comprises a comparative study of high-entropy metal-sublattice nitride, carbide, and boride thin films based on the equimolar material system HfTaTiVZr in terms of irradiation resistance. The samples were synthesized by reactive (carbide, nitride) and non-reactive (boride) magnetron sputtering in a lab-scaled PVD system. To simulate the damage caused by radiation, He implantation experiments were carried out within a He ion microscope on our films following investigations concerning its effects on their microstructure and mechanical properties.

2 Experimental

2.1 Sample synthesis

The synthesis of our samples was carried out at TU Wien by reactive as well as non-reactive magnetron sputtering. All depositions were conducted in DC mode on polished sapphire $(1\bar{1}02)$ wafers. The substrates used were ultrasonically cleaned in acetone followed by ethanol for a total of 10 minutes before installation inside the vacuum chamber with the polished sides facing the target. The deposition parameters used are based on previous research work on identical or very similar material systems [7, 16, 17]. The deposition times were chosen in a way to make sure we reach film thicknesses of around 3 µm which were needed to perform the planned experiments.

2.1.1 (HfTaTiVZr)C

The carbide samples were synthesized by reactive magnetron sputtering from an equiatomic powder-metallurgically prepared HfTaTiVZr Target (75 mm in diameter and 6 mm thickness, Plansee Composite Materials GmbH) in an argon-acetylene ($Ar - C_2H_2$) gas mixture using a lab-scale PVD system designed for the deposition of transition metal carbides by reactive magnetron sputtering. The target-substrate distance was set to 70 mm and rotation was applied to the substrate holder during deposition. Substrate etching with Ar-ions was done after reaching a base pressure below 0.5 mPa at the desired substrate temperature (450 °C) for 10 minutes by applying a -800 V DC bias voltage at an Ar gas pressure of around 4.9 Pa. Following this, a smooth transition to deposition is performed with sputter-cleaning of the target surface for 3 minutes and a subsequent opening of the shutter. During the deposition time of 40 minutes the target DC power density was around 5.8 W/cm^2 combined with a -22 V DC floating bias. The total gas flow of the argon-acetylene (Ar-C_2H_2) mixture was set to 20 sccm resulting in a process pressure of 0.33 Pa while the reactive gas flow-rate-ratio $f_{C2H2} = F_{C2H2} / (F_{Ar} + F_{C2H2})$ was 20 %.

2.1.2 (HfTaTiVZr)N

For the deposition of the nitride as well as boride films a modified Leybold Heraeus Z400 PVD system was utilized.

The synthesis of the nitride samples was conducted reactively in an argon-nitrogen (Ar-N_2) gas mixture at a flow-rate-ratio $f_{N2} = F_{N2} / (F_{Ar} + F_{N2})$ of 45 % from the identical target

as the carbide films. Between the carbide and nitride depositions the target was sand-blasted and subsequently cleaned further by a sputter plasma to prevent unwanted contaminations. The target-substrate distance was set to 40 mm. Substrate etching was done after reaching a base pressure below 0.3 mPa at the desired substrate temperature (440 °C) for 10 minutes with Ar-ions by applying a pulsed -150 V DC bias (pulse frequency = 150 kHz, pulse duration = 2496 ns) at an Ar gas pressure of around 1.3 Pa. Directly before opening the shutter a sputter-cleaning of the target surface was performed for 3 minutes. During the deposition time of 30 minutes the target DC power density was around 9.7 W/cm^2 while a -50 V DC bias was applied. The total gas flow of the Ar-N_2 mixture set to 40 sccm resulting in a pressure of around 0.44 Pa..

2.1.3 (HfTaTiVZr)B_2

The boride films were prepared non-reactively by magnetron sputtering from an equiatomic powder-metallurgically prepared (HfTaTiVZr)B_2 compound target (75 mm in diameter and 6 mm thickness, Plansee Composite Materials GmbH) in a Leybold Heraeus Z400 PVD system. The same target-substrate distance as well as pre-deposition procedure as for the nitride was used. During the deposition time of 30 minutes the target DC power density was around 5.9 W/cm^2 while a -50 V DC bias was applied. The total gas flow of the Ar-N_2 mixture set to 30 sccm resulting in a pressure of around 0.35 Pa while the substrate temperature during deposition was 440 °C.

2.2 X-ray diffraction

X-ray diffraction (XRD) measurements were performed at the X-Ray Center of TU Wien on a PANalytical X'Pert MPDII in Bragg-Brentano configuration using Cu-K_α radiation wavelength.

2.3 Energy-dispersive X-ray spectroscopy

An Oxford Instruments (UK) Xplore energy-dispersive X-ray spectroscopy (EDS) detector was used inside a Scios II Dual Beam (Thermo-Fisher, USA) FIB-SEM to obtain the chemical composition of our samples. For every one of our films, we conducted five measurements on different regions on the samples at acceleration voltage of 30 kV and beam current 3.2 nA.

The principle is based on the emission of characteristic X-rays resulting from electrons hitting the inner shells of the atoms. The energy of this X-rays is unique to each element.

An EDS detector converts this characteristic energy into electric voltage and by this the received signals are displayed in a spectrum using a designated software as shown in Fig. 1. The counts, respectively the peak height, at the different characteristic energy lines of the elements present in the sample is then used to calculate the composition of a sample.

A general concern with this technique for samples with a large number of elements is the overlapping of peaks which complicates the analysis. This issue is less of a concern for our case, as we have at least one standalone peak for each element (see Fig. 1). It is also known that the accurate quantification of lighter elements can be challenging even when with modern ultrathin-window EDS detectors, as used in our measurements. The problem is that the absorption of the already lower energy X-rays in the sample itself or the detector window reduces the signal that reaches the detector. Additionally, the weaker signals can be obscured by the background radiation more easily.

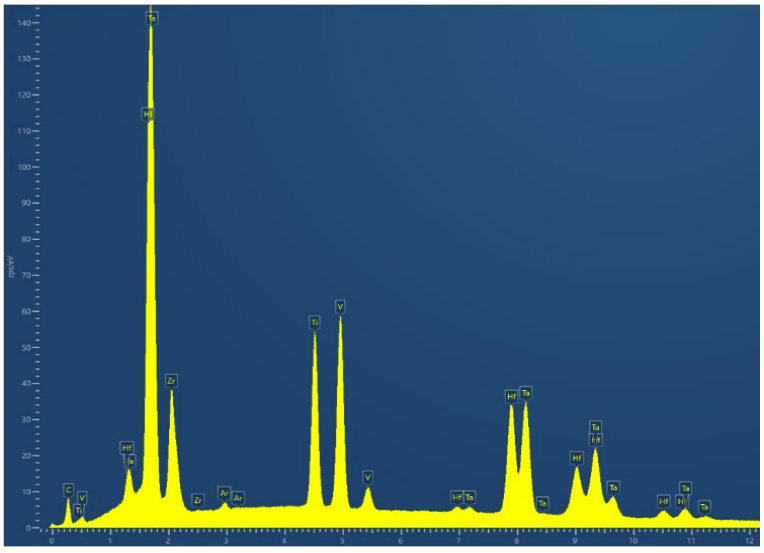

Fig. 1 Example EDS spectrum of a HfTaTiVZr carbide.

2.4 Helium implantation

To simulate surface near damage arising from irradiation environments, He ion implantation has been used for the decades now. A rather new approach in this field is the use of He ion microscopy (HIM) instead of large-scale ion accelerators or plasma generators. This allows for a much higher precision in terms of ion implantation parameters which is of great importance to sufficiently analyze the influence on different material properties. The downside can be the limitation to small volumes as the beam energy in a HIM is generally low and by that also the penetration depth [15].

For our experiments, He implantation was done inside a He-ion microscope (HIM, Orion Nanofab, Carl Zeiss GmbH) in combination with a NanoPatterning and Visualization Engine (NPVE) software (Fibics, Inc.) at ion energies of 25 keV and fluences of 5×10^{16}, 1×10^{17}, 2×10^{17} and 5×10^{17} ions/cm^2 in 8 × 8 µm^2 square patterns (pixel spacing = 0.5 nm, pixel dwell time = 1 µs) on the as deposited sample surfaces. The boride and carbide films were exposed to even higher ion fluences of up to 8×10^{17} and 1.2×10^{18} ions/cm^2 as they did not show surface blistering at the lower He doses.

2.4.1 Stopping Range of Ions in Matter

The He implantation experiments have additionally been simulated using the "Stopping Range of Ions in Matter" (SRIM) [18] software utilizing the Kinchin-Pease model. By this we get an insight into the depth distribution and amount of He within our samples as well as the displacements per atom (dpa). The dpa value is commonly used to quantify radiation damage and it essentially tells us how many times, on average, an atom has been knocked out of its place in the crystal lattice by radiation.

2.5 Atomic force microscopy

A Nanoscope III (Digital Instruments, USA) atomic force microscope (AFM) was used to analyze the surface topography in selected regions of our thin films upon He implantation. The data obtained by the AFM was processed with the Gwyddion [19] software to quantify the surface roughness as well as plateau height and thus volumetric swelling of the implanted areas.

2.6 Nanoindentation

To characterize the mechanical properties of our as deposited, as well as irradiated sample regions, nanoindentation measurements in continuous stiffness mode (CSM) were performed on a TI 950 Triboindenter (Hysitron Inc., USA). The CSM technique provides continuous measurements of stiffness throughout the indentation by overlaying the usual loading curve with a much smaller dynamic load. This allows the measurement of depth-dependent properties from a single indentation measurement. A "shot gun" approach was used to measure the hardness of the small, implanted surface regions (8 x 8 µm^2) by programming indentation arrays (at least 7 x 7 indents) with a minimum indent spacing of 2 µm. These arrays then covered the implanted areas as well as unaffected regions close by, giving us a direct comparison between the two states. This method allowed us to get at

least 7 indents per material state, confirmed by optical and SEM imaging. The maximum indentation load was 10 mN resulting in indentation depths of around 100 to 120 nm. These are reasonable depths concerning the indentation spacing, which should be at least 10 times the depth as suggested in [20], as well as surface roughness, which should be below 5% of the depth as suggested in the international standard ISO 14577-1 [21].

Care should be taken in interpreting the resulting data of these measurements as outright hardness and modulus values of our samples at a certain He dose because of various effects that come into play during a nanoindentation measurement [22]. Probably the most relevant in our case is the size of the affected and thus characterized area, which is significantly larger than the indentation size and presumably surpasses the penetration depth of the He ions. Also, the number of measurements per material condition is limited within this work due to the restricted size of the irradiated windows. Nevertheless, these measurements give an insight in the effects of He implantation dose on the mechanical properties of the films and should rather be viewed as comparative values.

2.7 Electron microscopy

A Scios II DualBeam (Thermo-Fisher, USA) focused ion beam scanning electron microscope (FIB-SEM) was utilized for SEM-imaging, the preparation of pillars, micro-cantilevers and corss-section samples for transmission electron microscopy (TEM) investigations. Before cross-section preparation a protective layer was deposited using Pt as a precursor material.

To characterize the microstructure in the irradiated regions of our samples TEM and scanning-TEM (STEM) analyses were conducted with a TitanX microscope (FEI, USA) operated at 300 kV. Additionally, the same FIB-SEM as used for the preparation of the cross-sections was used for STEM imaging.

2.8 Pillar compression

2.8.1 Preparation

As shown in Fig. 2, pillars were prepared with a Scios II DualBeam (Thermo-Fisher, USA) FIB-SEM on sample fracture edges oriented perpendicular to the film surface. The pillars were milled to a square cross-section with a side length of 300 nm and a height of 1200 nm. We were able to reproduce these dimensions with an error of below 10 nm, measured by SEM imaging. It should be noted that owing to the ion milling process it is

not possible to produce a perfectly rectangular shape. In reality, the pillars shape is closer to a very steep rectangular pyramid. This must be kept in mind during the analysis of the testing data. Ten pillars were milled and tested on each sample and half of them were subsequently implanted with He.

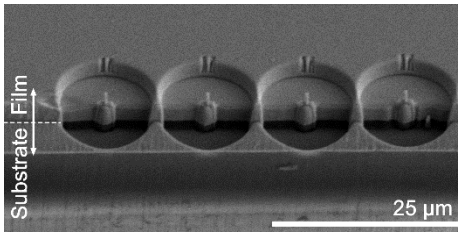

Fig. 2 Pillars prepared on sample fracture edge by FIB-milling.

2.8.2 He implantation

He implantation was again done inside the HIM mentioned in section 2.4. The penetration depth of 25 keV He ions is around 180 nm if implantation is done perpendicular to the sample surface, as confirmed by SRIM calculations and STEM cross-section imaging. To still be able to implant the entire height of our pillars we chose to implant the pillars in a two-step procedure from two opposing sides as shown in Fig. 3. The films were mounted flat on a standard 12.5 mm diameter SEM stub. As the stage tilt inside the HIM is limited to 54° we were not able to implant perpendicular to the pillar side surfaces. As a compromise we chose to implant at a stage tilt of 45° with a dose of 3e17 ions/cm^2 which yields to a equivalent "perpendicular" dose of 2.12 ions/cm^2 if accounted for the tilt.

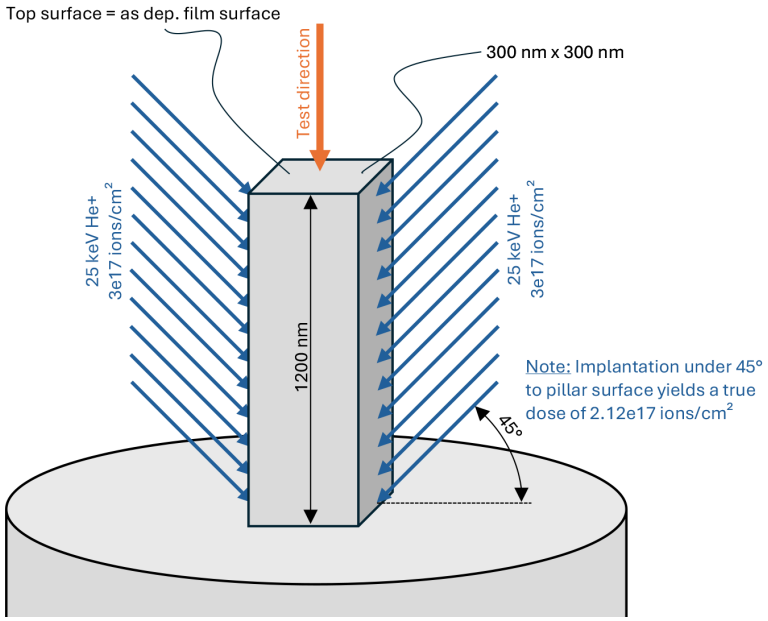

Fig. 3 Schematic illustration of our pillar implantation and testing setup.

2.8.3 Testing

A Femto Tools NMT04 in-situ nanoindenter equipped with a 5 µm diameter flat punch was used inside a SEM to conduct the compression tests at a displacement rate of 5 nm/s. Before and after SEM images of an exemplary pillar test are shown in

Fig. 4.

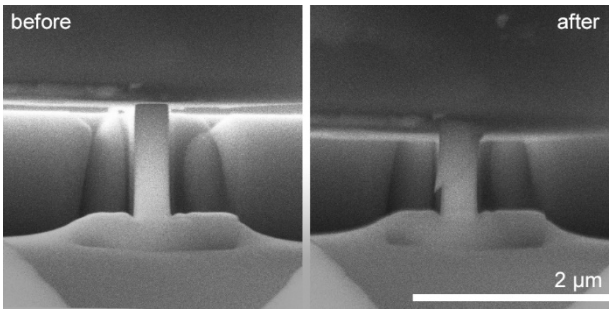

Fig. 4 Exemplary before and after SEM images of an in-situ compression test of our HfTaTiVZr boride thin film.

The loading curves resulting from the measurements were used to quantify the compression stiffness as well as the critical loads at which failure occurred.

2.9 Pre-notched micro-cantilevers

2.9.1 Preparation

Pre-notched micro-cantilevers for fracture toughness quantification were prepared on sample fracture edges by ion milling with a Scios II DualBeam (Thermo-Fisher, USA) FIB-SEM. For the final cuts the ion current was reduced to 10 pA at an acceleration voltage of 30 kV to reduce ion surface damage. The dimensions of the cantilevers (see Fig. 5) were chosen considering the findings presented in [23] and [24]. We are aware that the chosen size is at the lower end of what is reasonable leading to a somewhat heightened error in the results. The notch was milled at a current of 10 pA to achieve the lowest possible root radius. Marks were added to the tip and sides of our finished cantilevers to simplify the positioning of the Berkovich tip during the testing procedure.

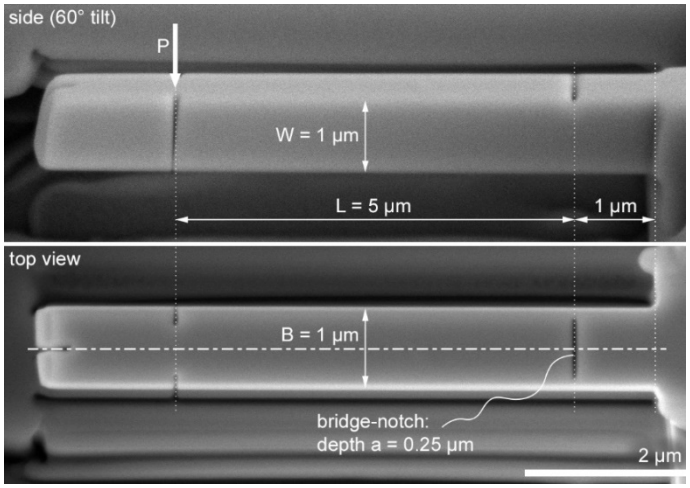

Fig. 5 Final dimensions of our pre-notched micro-cantilever prepared by FIB-milling on sample fracture edge.

2.9.2 Testing

A Femto Tools NMT04 in-situ nanoindenter equipped with a Berkovich tip inside a SEM was used to conduct the bending tests at a displacement rate of 30 nm/s. An exemplary testing procedure is shown in Fig. 6.

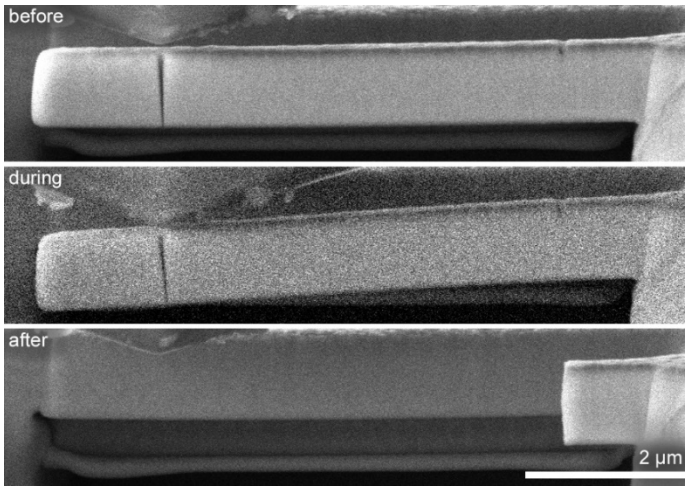

Fig. 6 In-situ testing procedure of our micro-cantilevers inside a SEM system using a FemtoTools nanoindenter equipped with a Berkovich tip.

The fracture toughness K_{IC} was calculated analytically using linear-elastic fracture mechanisms with the following formulars (Eq.1, Eq.2) proposed in [24].

$$K_{IC} = \frac{F_{max} L}{B W^{3/2}} f(\frac{a}{W}) \quad \text{(Eq. 1)}$$

$$f\left(\frac{a}{W}\right) = 1.46 + 24.36\left(\frac{a}{W}\right) - 47.21\left(\frac{a}{W}\right)^2 + 75.18\left(\frac{a}{W}\right)^3 \quad \text{(Eq. 2)}$$

Where F_{max} is the fracture load, L is the distance between notch and load introduction point, a is the notch depth, B is the width and W is the height of the cantilever. The fracture cross-section dimensions as well as notch depth a was measured by SEM imaging after testing.

3 Results and Discussion

3.1 X-ray diffraction

As displayed in

Fig. 7, all coatings possess a single solid solution phase. The nitride as well as carbide possesses a cubic unit cell, while the boride shows a hexagonal structure. The difference in lattice parameters between nitride (4.409 Å) and carbide (4.501 Å) can be attributed to the size difference of the interstitial nitrogen and carbon atoms. While the nitride shows a slightly preferred growth towards the (220) direction, the carbide is preferably oriented towards (111). In the boride clearly the basal plane growth direction (001) is predominant.

Looking at the nitride diffraction pattern in Fig. 7, there is a slight deviation from the perfect cubic unit cell visible in the (200), (311) and (400) directions. The peaks are shifted to higher values which could mean that there exists a very slight tetragonal distortion of the cubic.

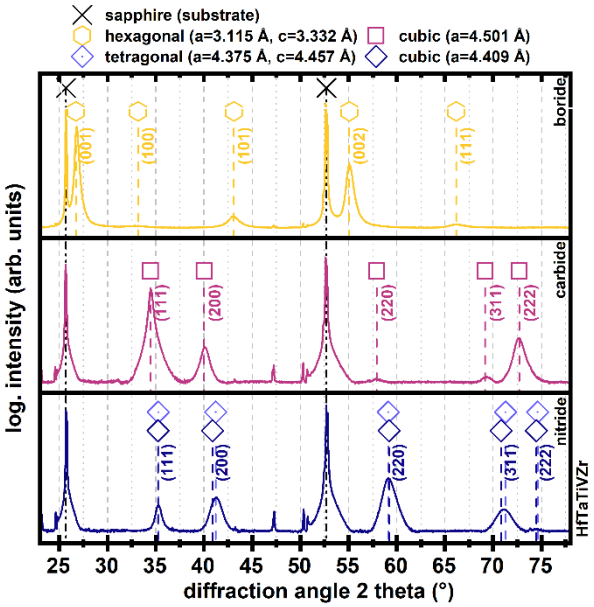

Fig. 7 X-ray diffraction patterns of our HfTaTiVZr nitride (bottom), carbide (center) and boride (top) thin films deposited with a substrate temperature of 450 °C. Reference data for a cubic phase with a lattice constant of 4.409 Å (diamonds), a tetragonal phase with a lattice constants of a=4.375 Å and c=4.457 Å (diamonds with center dot), a cubic phase with a lattice constant of 4.501 Å (cubes), a hexagonal phase with a lattice constants of a=3.115 Å and c=3.332 Å (hexagons) as well as the sapphire (Al_2O_3) substrate (crosses) is indicated.

3.2 Chemical composition

The chemical composition of our thin films, obtained by top-down SEM-EDS, is displayed in Fig. 8 and Tab. 1.

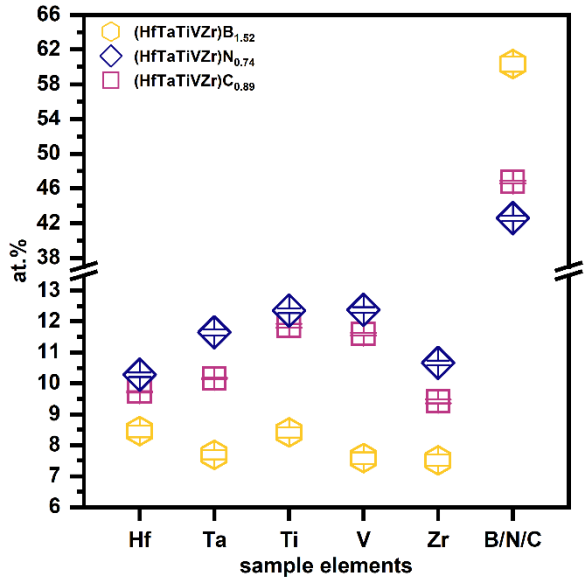

Fig. 8 Chemical composition of our HfTaTiVZr boride (hexagons), nitride (diamonds) and carbide (cubes) thin films, obtained by SEM-EDS.

The metallic elements are roughly equally distributed, as it can be expected from the equimolar compositions of the sputter targets. Variations from the target composition are known to occur from the nature of the sputter principle [25]. The films are consistently under-stoichiometric, which can most likely be explained by vacancies in the non-metallic sublattices.

	Chemical composition [at%]					
	Nitride	**Error**	**Carbide**	**Error**	**Boride**	**Error**
Hf	10.28	0.07	9.73	0.03	8.45	0.19
Ta	11.65	0.09	10.16	0.02	7.69	0.15
Ti	12.35	0.08	11.86	0.07	8.42	0.17
V	12.38	0.09	11.60	0.04	7.59	0.19
Zr	10.66	0.07	9.42	0.06	7.52	0.18
N	42.56	0.30				
C			46.74	0.15		
B					60.33	0.87
Ar	0.11	0.08	0.49	0.02	0.00	0.00
Stoichiometry	0.74		0.89		1.52	

Tab. 1 Chemical composition of our HfTaTiVZr boride (hexagons), nitride (diamonds) and carbide (cubes) thin films, obtained by SEM-EDS.

3.3 Fracture cross-sections

The fracture cross-section images represented in Fig. 9 provide an insight into the growth morphology of the as-deposited films as well as the achieved film thicknesses. The deposition rates were calculated to be 81.5 nm/min (2.44 µm; 30 min) for the nitride, 88.1 nm/min (2.64 µm; 30 min) for the boride and 90.2 nm/min (3.62 µm; 40 min) for the carbide. While all samples possess a somewhat fibrous microstructure, clear differences can still be observed in the fracture surfaces of the films. Most obviously the boride appears much finer grained compared to the other two samples. Unlike the other two films, which show clear columnar grains, the nitride sample possesses rather interrupted columns which could be attributed to recurrent nucleation during the growth process.

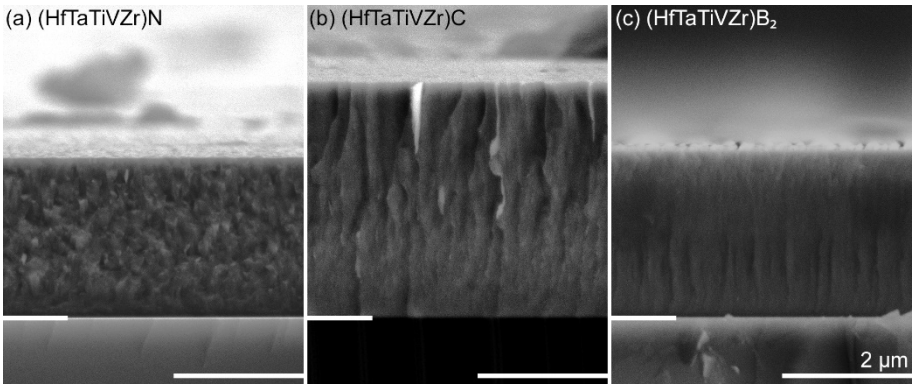

Fig. 9 Fracture cross-sections of our HfTaTiVZr (a) nitride, (b) carbide and (c) boride thin films. The white bar in the lower right corner of each image represents a length of 2 µm while the bar on the left side marks the interface between film and substrate.

3.4 Helium implantation/swelling

The results of SRIM calculations for 25 keV He ions at a dose of 5e17 ions/cm^2 are displayed in Fig. 10. Due to their elemental similarity and thus roughly similar densities, the differences between the three compositions are rather small. We can see a slightly higher maximum penetration (about 10 nm higher) depth for the carbide compared to the other compositions and the calculated dpa values are the lowest for the boride.

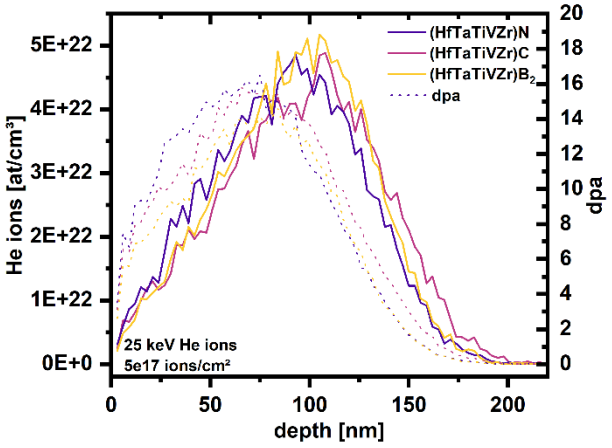

Fig. 10 Results of SRIM simulations for 25 keV He ion implantation to a dose of 5e17 ions/cm^2

The roughness values (Ra, Rz) of our films measured by AFM are displayed in Fig. 11 and agree with the observations in regard to microstructure from the fracture cross section images (see Fig. 9). The comparably low surface roughness of the boride film could originate from the very strongly oriented growth in the basal plane direction [26], as discovered in the XRD diffraction pattern in

Fig. 7. The increased roughness of the nitride and carbide coatings should be kept in mind when looking at the swelling values of those films, particularly at the lower values, and is also reflected in the error bars.

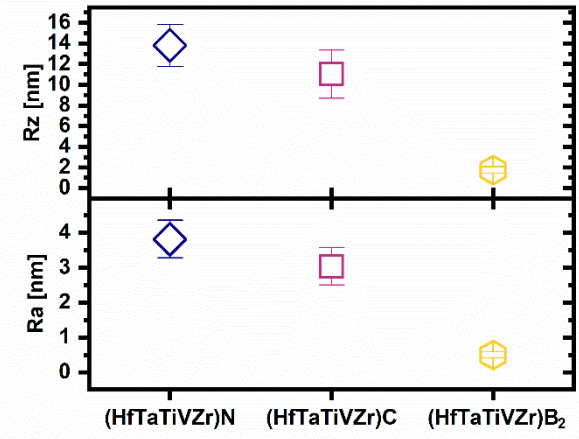

Fig. 11 Roughness values (Rz; Ra) of our HfTaTiVZr nitrides (diamonds), carbides (cubes) and borides (hexagons).

The results of the He implantation experiments in terms of volumetric swelling are displayed in Fig. 12. Generally, the differences in swelling of the nitride, carbide and boride films are rather low and comparable to that of tungsten [15] or lower. The measured values at a He dose of 5e17 ions/cm^2 sorted upward are 10.72±1.20 % (18.79±2.13 nm of 177 nm) for the nitride, 11.71±0.47 % (20.72±0.83 nm of 177 nm) for the boride and

15.12±0.75 % (28.13±1.40 nm of 186 nm) for the carbide. This sequence can also be observed in the dose at which the first surface blisters can be observed where the lowest swelling nitride showed the first blistering at the lowest dose (~3.8e17 ions/cm²) followed by the boride (~6.5e17 ions/cm²) and carbide (~8e17 ions/cm²) films. These observations suggest that for example the carbide can absorb the highest amount of He and thus shows the highest volumetric swelling while the critical dose for blistering is the highest here as well. The opposite is true for the nitride and the boride is in between.

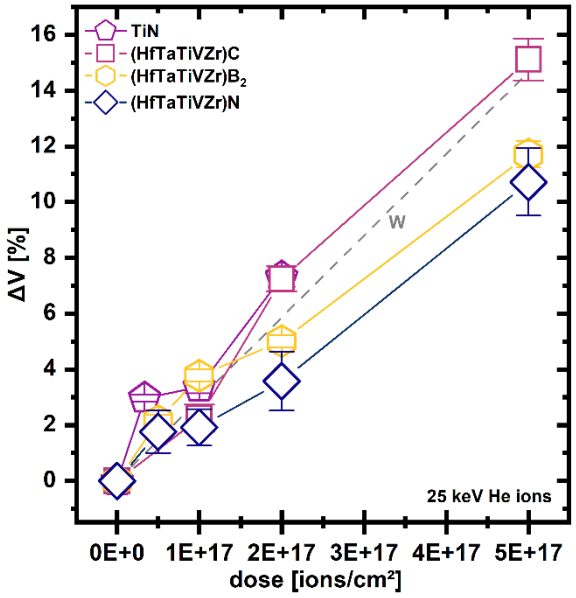

Fig. 12 Percentage of volumetric swelling of our HfTaTiVZr carbides (cubes), borides (hexagons) and nitrides (diamonds) as well as Ti nitride (pentagons) depending on the implanted He dose, measured by AFM. A linear interpolation of the tungsten swelling value (taken from [15]) is displayed by the dash-dotted line.

The contour plots displayed in Fig. 13 exemplarily show the development of the surface swelling and finally blistering upon He implantation into our boride thin films.

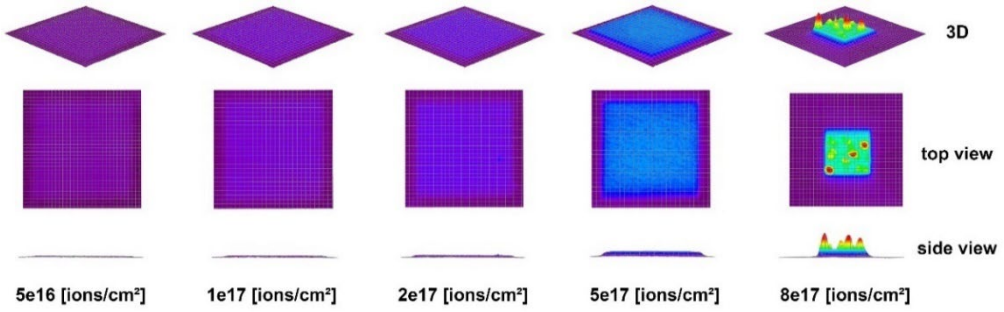

Fig. 13 3D contour plots of our HfTaTiVZr borides after He implantation, obtained by AFM.

Different modes of blistering were observed in the different thin films as visible in the SEM images of the He implanted areas in Fig. 14. Please note that the He dose and the stage of blistering is not identical for the different samples in these images. While the nitride (Fig. 14a) shows a larger number of smaller blisters the carbide (Fig. 14b) and boride (Fig. 14c) films possess parts of the implanted fields which seem almost unaffected by the blistering. This is most prominent for the carbide sample, and we suspect this is connected to an easier He diffusion on the closest packed (111) plane, which was most pronounced in the XRD diffraction patterns of this film. It looks as if the boride is more brittle as more of the blisters crack open before they start to grow larger.

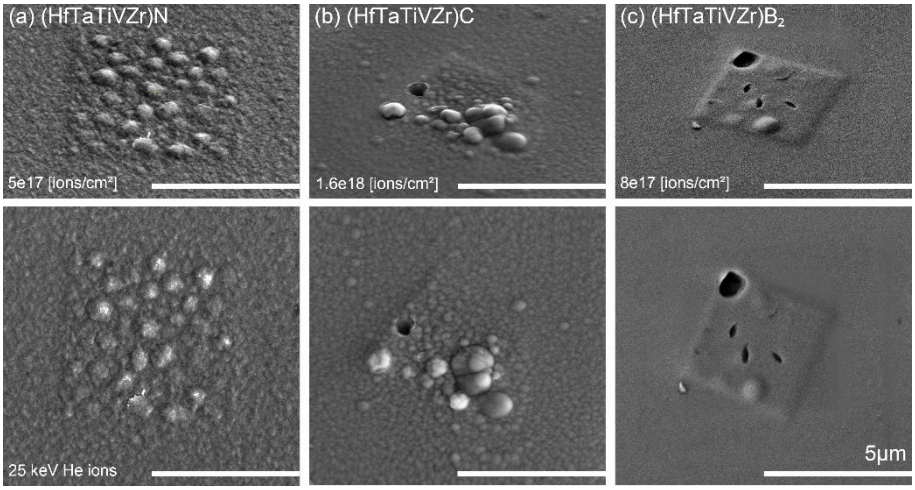

Fig. 14 Different modes of blistering observed on our HfTaTiVZr (a) nitride, (b) carbide, and (c) boride thin films. Please note that the He dose and the stage of blistering is not the same on all samples.

3.5 Nanoindentation

The results of the nanoindentation measurements on the He implanted regions of our thin films are shown in Fig. 15. The hardness / elastic modulus of our nitride, carbide and boride films in the unirradiated state were 26.9±1.3 / 372.1±14.1 GPa, 32.4±1.5 / 409.6±13.5 GPa and 38.9±0.7 / 435.3±5.6 GPa. Apart from the nitride at the lowest tested dose, it is clear that the mechanical properties degrade for all samples with the He dose respectively volumetric swelling. This makes sense for our case of ceramic materials which usually only show very little or no strain hardening due to their incapability to deform through dislocation movement. It has been found for Cu [27] that the hardness increases initially and then starts to decrease at higher He doses. There, it was proposed that, the He microbubbles first act as obstacles for dislocation movement until they get

large enough so that the material starts to behave like a nanoporous material and thus sees a decrease in hardness. The amount of swelling in our films is inversely proportional to the decrease in hardness and elastic modulus. At a He dose of 5e17 ions/cm^2 the relative decrease in hardness / elastic modulus sorted upwards is -20.1±1.7 / -13.8±1.4 % for the boride, -27.5±6.2 / -14.9±4.7 % for the nitride and -38.2±7.5 / -30.6±6.8 % for the carbide. This agrees with our conclusion after the swelling measurements, that the carbide absorbs the highest amount of He, as the degradation in the mechanical properties is the highest of all three tested compositions.

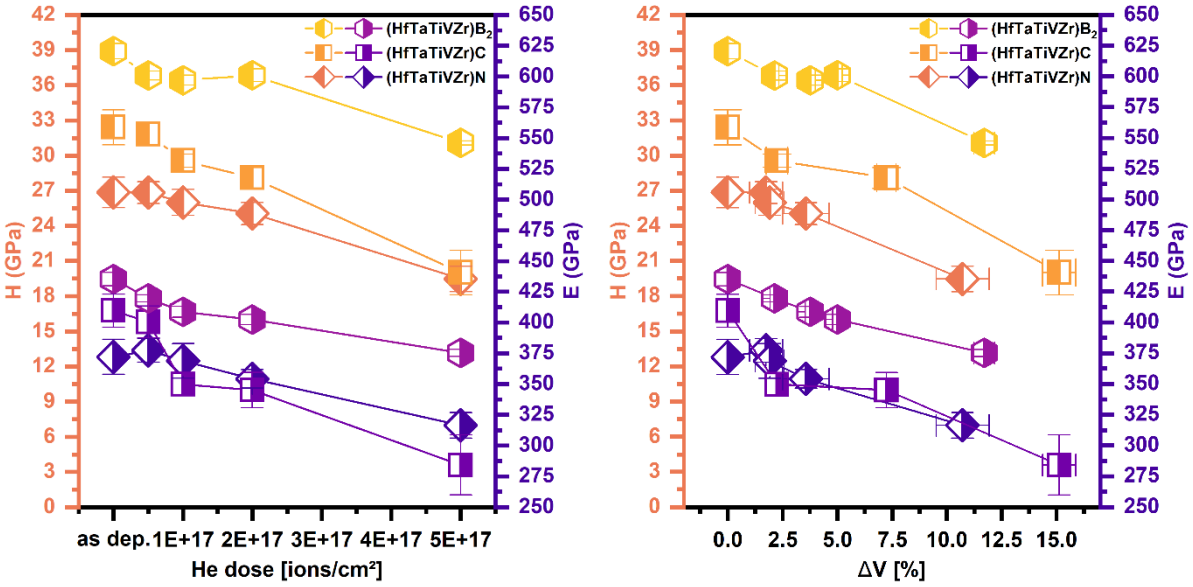

Fig. 15 Hardness and elastic modulus of our HfTaTiVZr boride, carbide and nitride thin films in the as deposited state as well as irradiated with different doses of He (left – H,E over He dose; right – H,E over ΔV).

Basically, the He absorption can be viewed as an increase in free space in the microstructure of the film which obviously decreases the hardness and stiffness of the material. This hypothesis can be supported by calculations of the elastic modulus based on the amount of volumetric swelling. A micromechanical model was applied in [28] to relate the free space inside a material to the elastic modulus. As a result, Lu et al. propose the following simple formula (Eq. 3) for materials with a porosity lower than 30%.

$$E = E_0(1 - 2\Phi)(1 + 4\Phi^2) \qquad \text{(Eq. 3)}$$

Where E_0 is the elastic modulus for a porosity value of zero and Φ is the porosity.

This formula was used to calculate the decrease in elastic modulus for our samples based on the volumetric swelling, obtained by AFM measurements and SRIM simulations. The results of these calculations, shown in

Fig. 16, are in exceptionally good agreement with the measured values in case of the nitride and boride sample. The carbide loses more stiffness than the model would suggest, at least for the higher He doses.

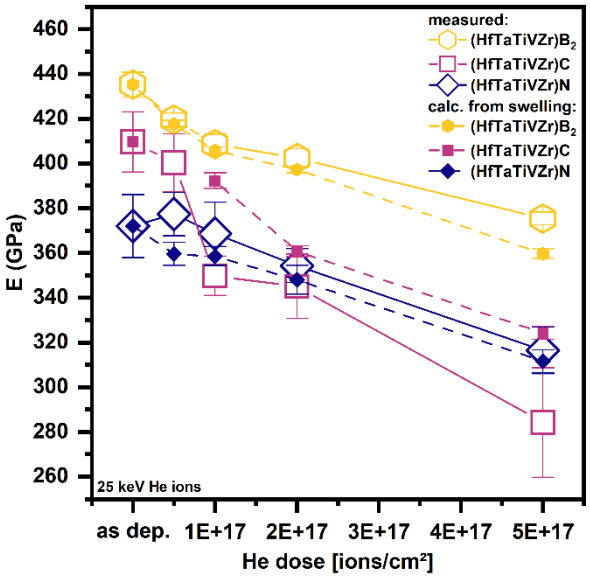

Fig. 16 Elastic modulus of our HfTaTiVZr boride, carbide and nitride thin films in the as deposited state as well as irradiated with different doses of He measured by nanoindentation as well as calculated from the volumetric swelling by a micromechanics model proposed in [28]

3.6 TEM cross-sections

To get a sense of how the He affects the microstructure of our films, cross-section lamellas were cut out of the He implanted. STEM images of our film's microstructures after He irradiation at a dose of 5e17 ions/cm^2 in Fig. 17 and Fig. 18. Very interestingly, despite great compositional similarity, they show very different responses to the identical irradiation treatment. While we see very finely distributed nanobubbles in the boride (Fig. 17a) we already see linking up of the bubbles in large crack for the carbide (Fig. 17b). There we can also clearly see that He accumulates at the grain boundaries favoring crack propagation, not only within, but also in between the columnar grains. The nitride (Fig. 17c) has already reached the next stage of degradation as the crack has already formed a blister. This occurs as more and more He gas accumulates in the crack cavity thus forming a dome that is then visible on the samples surface (see Fig. 14). The growth of a blister stops

as it cracks open thus releasing the excess gas. As in the carbide we also see the grain boundaries acting as sinks for the He accumulation in the nitride and thereby cracks forming between the grains.

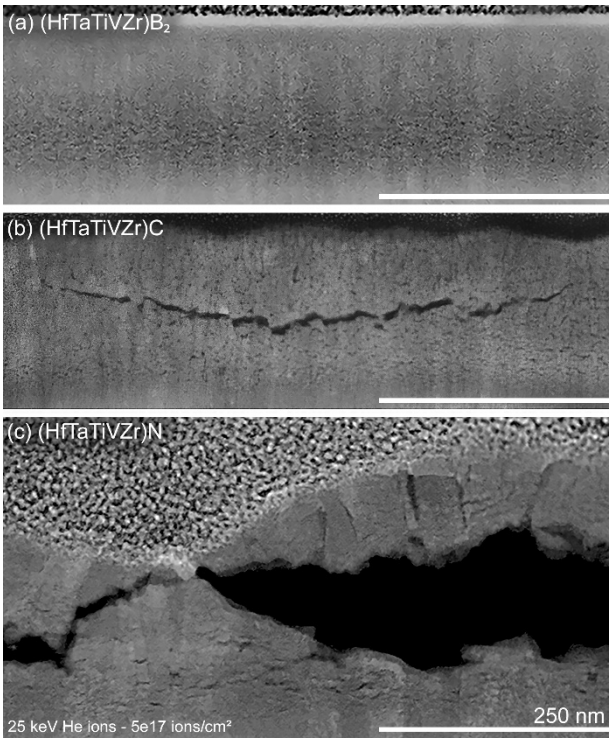

Fig. 17 STEM dark field images of the microstructure of our HfTaTiVZr (a) boride, (b) carbide and (c) nitride thin films upon 25 keV He implantation at dose of 5e17 ions/cm^2.

In Fig. 18 we have overlayed the results of the SRIM calculations with the STEM cross-section images. There we see that the calculated depth at which the maximum He content is present agrees well with the depths at which the larger cracks form in the images. Also, the calculated maximum penetration depth of the He matches with the observations in the STEM. It has to be kept in mind that the SRIM software does not account for the swelling and thus the density-decrease during the implantation process. We can see that very clear in Fig. 18a where the offset between the calculated peak of the He content and the larger crack is about 15 nm which agrees well with the measured swelling values at the respective dose.

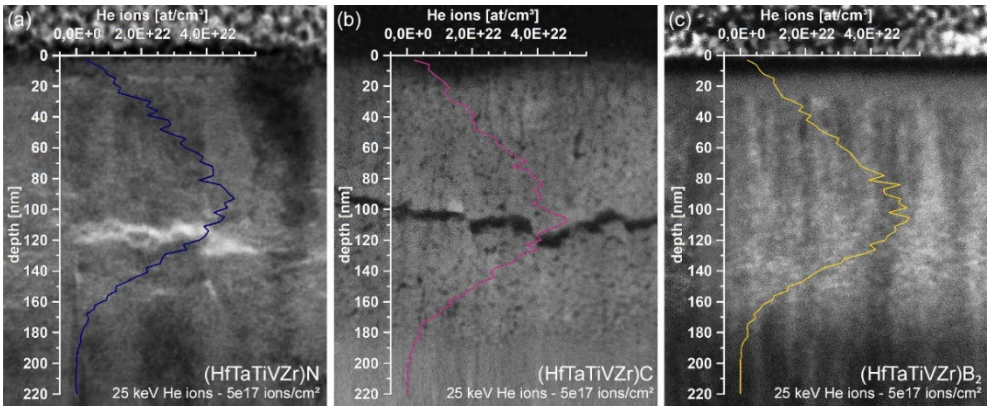

Fig. 18 Comparison of microstructure overlayed with SRIM calculations (not accounted for swelling) of our HfTaTiVZr (a) nitride (bright filed), (b) carbide (dark field) and (c) boride (bright field) thin films upon 25keV He implantation at dose of 5e17 ions/cm^2.

More STEM images are displayed in Fig. 19, Fig. 20 and Fig. 21 showing blistering occurs also for the boride and carbide, but is delayed to higher He doses.

In Fig. 19b we can see a very clear example of the grain boundary weakening effect as there are cracks formed in between the columnar grains perpendicular to the expected crack propagation direction from the blister formation.

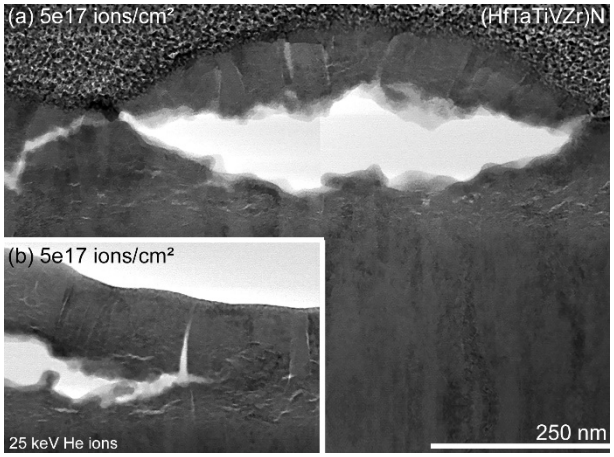

Fig. 19 STEM cross-section images of our HfTaTiVZr nitride thin film implanted with 25 keV He ions to a dose of 5e17 ions/cm^2.

At a higher dose of 1.2e18 ions/cm^2 the microstructure of our carbide film (Fig. 20a) is riddled with cracks and blisters in the He affected region. Interestingly, the regions left and right of the large blister seem to be somewhat depleted of cracks. We suspect this is connected to the He diffusing into the large cavity and thus less He is present adjacent to it.

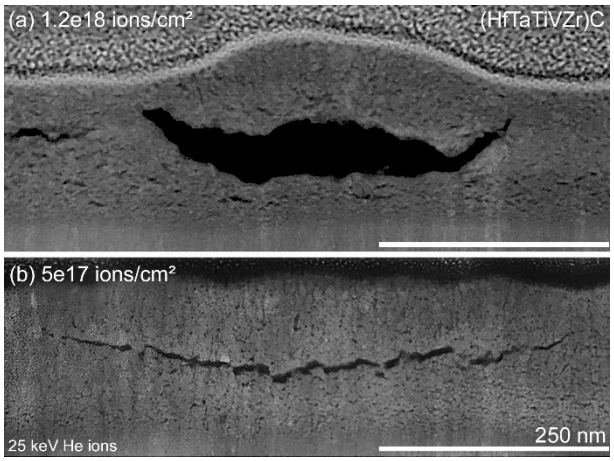

Fig. 20 STEM cross-section images of our HfTaTiVZr carbide thin film implanted with 25 keV He ions to a dose of (a) 1.2e18 and (b) 5e17 ions/cm^2.

For the boride we were not able to produce surface blisters consistently (Fig. 21a). At the same He dose we sometimes saw blisters form (Fig. 21b) but most of the times we just got visible cracks on the surface. We suspect that the very high hardness and modulus of this sample lower the likelihood of the blister dome formation because cracks reach the surface and thus release the overpressure inside the respective void.

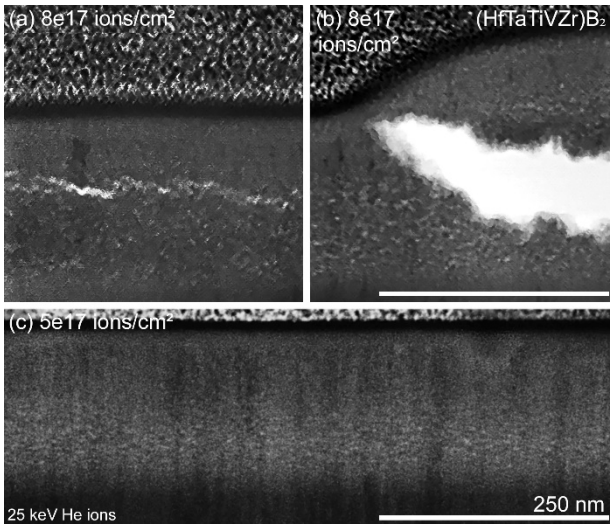

Fig. 21 STEM cross-section images of our HfTaTiVZr boride thin film implanted with 25 keV He ions to a dose of (a), (b) 8e17 and (c) 5e17 ions/cm^2.

The SAED patterns in Fig. 22 show that our samples remain crystallin even upon He implantation to a dose where we saw blisters occur.

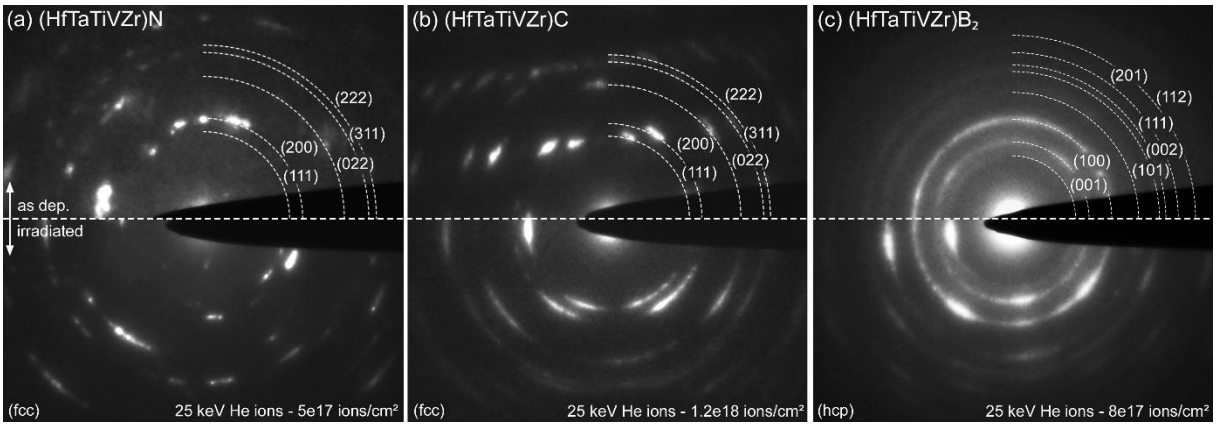

Fig. 22 SAED patterns of our HfTaTiVZr (a) nitride, (b) carbide and (c) boride thin film in the as deposited as well as He ion irradiated state.

3.7 Pillar compression testing

Pillar compression testing revealed different behaviors between our HfTaTiVZr nitrides, carbides and borides regarding stiffness, deformability, and failure. A selection of characteristic load-displacement curves is plotted in Fig. 23 where the distinct behavior of each ceramic becomes visible. While the nitride exhibits a comparably ductile behavior, the carbide and boride possess a brittle nature, where the carbide shows some plasticity before failure which is not present in the boride. Next to the as deposited state we also tested pillars irradiated with He to a dose of 2.12e17 ions/cm^2. As pictured by the dash-dotted lines in Fig. 23, the general characteristic of each ceramic remains present upon He implantation while the measured load, displacement and stiffness values decrease significantly. This can be attributed to the presence of microbubbles in the pillars, which weaken the ceramics and act as fracture initiation points.

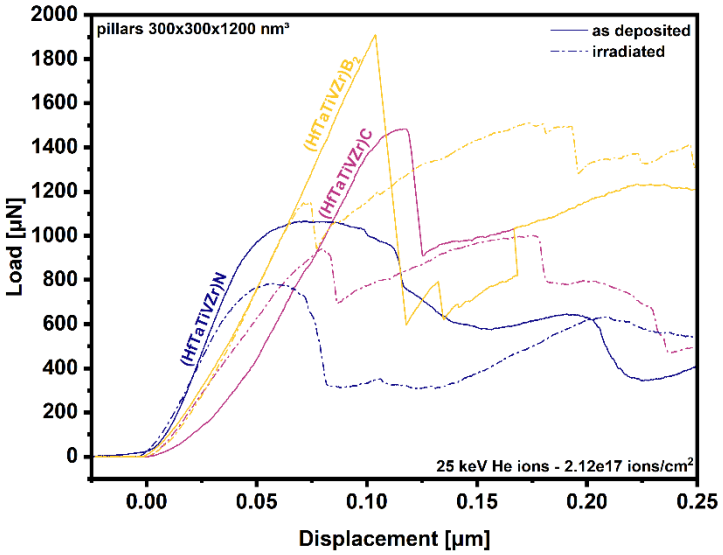

Fig. 23 Characteristic load-displacement curves of our as deposited (solid lines) as well as He irradiated (dash-dotted lines) HfTaTiVZr boride, carbide and nitride thin film pillar compression tests.

The He concentration profile across the pillar width resulting from a two-sided implantation (25 keV – 3e17 ions/cm²) at an angle of 45° to the side surfaces calculated using the SRIM [18] software is displayed in Fig. 24.

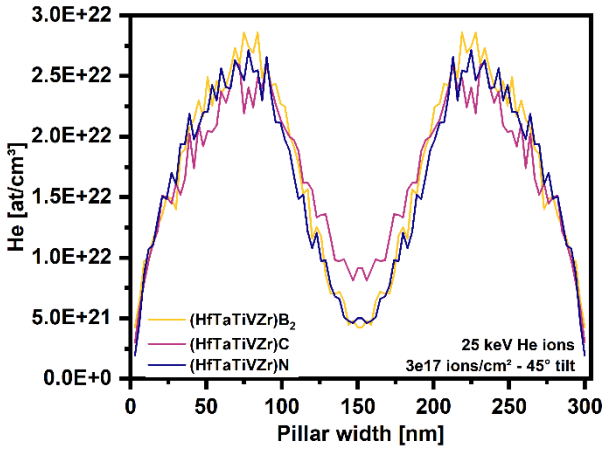

Fig. 24 Results of SRIM simulations for 25 keV He ion implantation under 45° stage tilt from two sides to a dose of 3e17 ions/cm².

Two exemplary and typical SEM images of our pillars after testing are displayed in Fig. 25. There were two main failure modes that we observed over all of the conducted tests which were either shear failure (Fig. 25a) or the formation of cracks (Fig. 25b), presumably at the grain boundaries. Looking at all the tests, there seems to be a slightly higher tendency towards shear failure instead of cracking after He irradiation.

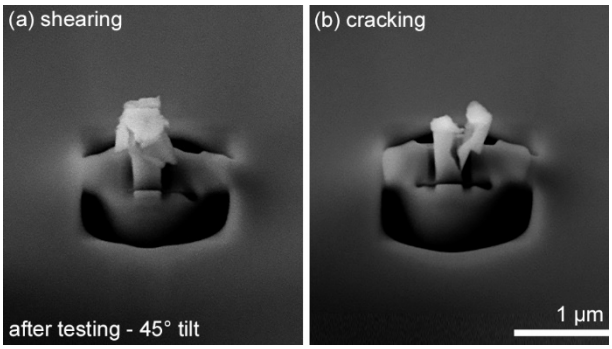

Fig. 25 SEM images of our pillars recorded after testing. The two main failure modes observed over all tested pillars were (a) shearing and (b) cracking.

The critical strain and stress values in as-deposited as well as irradiated state resulting from the analysis of the load-displacement curves are summarized in Fig. 26. The FemtoTools Suite (FemtoTools, Switzerland) software was used for the graph analysis. To characterize the behavior of the pillars, the yield point, the point of the ultimate load and

the point of the first abrupt failure were evaluated. For the calculation of the strain, stress and modulus values, an initial pillar height of 1200 nm and a cross section surface of 90000 nm^2 (300 nm x 300 nm) were assumed. This is reasonable as we were able to produce the pillars to a consistent high accuracy. As mentioned earlier, the pillars have a slightly pyramidal shape arising from the ion milling process. Unfortunately, due to the small size of the pillars, it was not possible to measure the individual cross sections with sensible precision. Yet, the assumed cross section is very close to the real values and thus a good assumption.

Looking at Fig. 26 it becomes immediately obvious that the strain as well as stress values consistently decrease upon irradiation. The microstructural defects introduced by the He ion irradiation act as dislocation initiation spots or enable grain boundary slipping at lower loads compared to the unirradiated samples. Failure occurs at lower stresses and strains after irradiation which can also be connected to microporosity which causes stress peaks and thus produces fracture initiation points. At a very close look the ultimate strain and failure strain consistently move closer together for the nitride and carbide upon irradiation. The opposite is true for the yield strain and ultimate strain which move slightly further apart. This could be connected to successively collapsing voids.

As expected merely because of its hexagonal crystal structure, failure occurs without visible ductility in the boride sample.

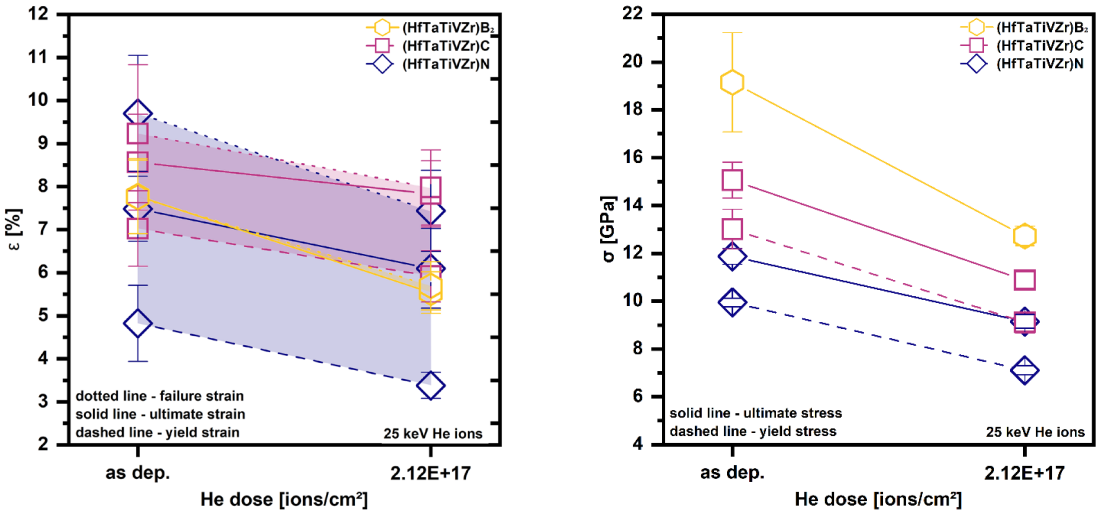

Fig. 26 Critical strain and stress values of our HfTaTiVZr boride, carbide and nitride thin film pillar compression tests obtained from the corresponding load-displacement curves.

The compression modulus values calculated form the slope of the loading curve are summarized in Fig. 27. While the nitride and boride sample undergo only a very slight

decrease of stiffness upon He ion irradiation to a dose of 2.12e17 ions/cm^2, the carbide shows a very clear degradation. This result is very consistent with our nanoindentation experiments as illustrated in Fig. 27. The compressive modulus is expectedly lower than the indentation modulus, but the relative trend upon irradiation remains the same for both experiments.

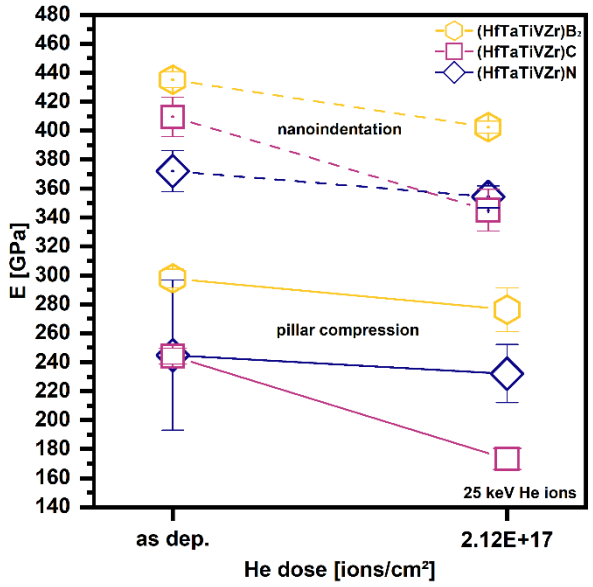

Fig. 27 Elastic modulus values of our HfTaTiVZr boride, carbide and nitride thin film pillar compression tests curves in comparison to the indentation moduli.

It should be mentioned that there is a general concern about pillar compression testing as there are many parameters which cannot be controlled or measured during such an experiment. Also, it must be kept in mind that due to the FIB milling process with 30 kV Ga ions used for the manufacturing of the pillars, there will always be some ion damage at least a few nanometers into the sample surface [29]. This can definitely have an influence on the measured values. To keep this influencing factor as small as possible the final cuts on our pillars were conducted with a low beam current of 10 pA.

It has already been shown in other research work [29] that the shape and size of the pillars have a significant influence on the outcomes of compression tests. For example, the pillar height matters, because of the continuous connection to the substrate which poses a strong constraint, usually not present in conventional compression tests. This constraint is expected to have a lower impact in taller pillars. Also, the aspect ratio of pillars should not be too high as buckling will become the main failure mode at some point. Lastly, the overall size of the pillars has shown to be significant where higher stress values and strain

hardening rates were measured with decreasing pillar size in [29]. This can be connected to dislocation mechanisms. Additionally, dimensional deviations in the tested structures have a greater effect the smaller their size, leading to a higher scatter in the results of the measurements.

3.8 Micro-cantilever fracture testing

The fracture toughness K_{IC} values displayed in Fig. 28 were calculated analytically using linear-elastic fracture mechanisms [24] upon evaluation of our recorded load-displacement curves and measurement of the fracture cross-sections after testing. While the nitride and boride coatings possess a fracture toughness of 2.83±0.03 and 3.47±0.14 MPa√m the carbide is the most brittle of the three with a value of 2.48±0.07 MPa√m. It seems likely that this finding is an explanation for the much stronger decrease in stiffness we discovered previously in our nanoindentation and pillar compression tests. We suspect that the carbide tends to form cracks, or grows existing cracks, in between the He microbubbles upon loading much easier than the other samples and thus shows a stronger depletion of modulus and hardness values.

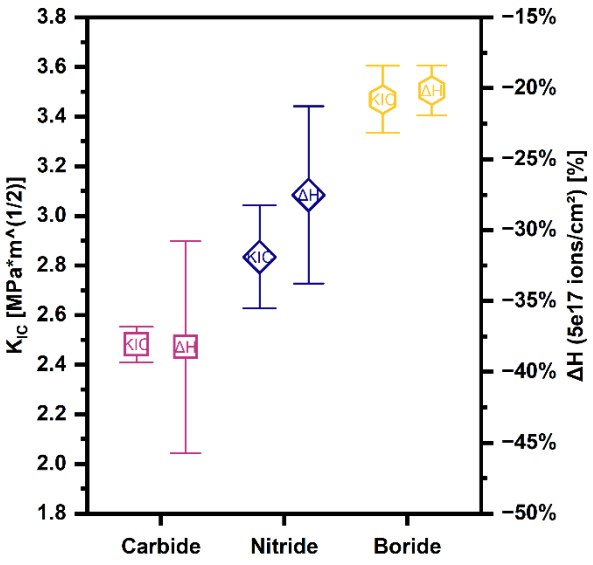

Fig. 28 Fracture toughness (left axis) as well as change of hardness upon He implantation at 5e17 ions/cm^2 (right axis) of our HfTaTiVZr carbide, nitride and boride thin films.

4 Summary and Conclusion

This work investigated the suitability of high-entropy metal-sublattice thin films composed of the refractory elements (Hf, Ta, Ti, V, Zr) – specifically nitrides, carbides, and borides – for first wall applications in nuclear fusion reactors. These materials offer promising properties, however, their long-term performance in a reactor necessitates a comprehensive understanding of their response to irradiation, a critical factor in the harsh fusion environment.

Employing He ion irradiation inside a He ion microscope, we observed distinct behaviors in the films, despite their similarities in the elemental composition. Carbide films exhibited significant volumetric swelling, resembling the behavior of W, a currently explored material for first wall applications. This swelling correlated with the most pronounced degradation in hardness and elastic modulus among the tested films. Conversely, nitride and boride films demonstrated superior resistance to irradiation damage, meaning less swelling and lower relative decrease in the mechanical properties making them a potentially more attractive pathway for fusion applications.

STEM imaging of our film's microstructures confirmed the previously proposed hypothesis of inter-crack formation within He microbubbles as the primary mechanism for void growth and thus degradation. Additionally, the study confirmed a weakening effect of He exposure on grain boundaries.

Micromechanics models were employed to estimate the decrease in modulus based on microporosity, yielding results that aligned well with measured values for all films except the carbide. This is likely to be connected to its low fracture toughness compared to the nitride and boride, which eases the crack propagation and thus disintegration of the microstructure upon loading.

These findings highlight the essential role of irradiation testing in identifying suitable first wall materials. Among the investigated compositions, the boride sample consistently demonstrated the most promising response to irradiation. This and the fact that there is very limited existing research on borides for nuclear fusion applications would make it a compelling candidate for further exploration.

5 List of references

[1] H. Bolt, V. Barabash, G. Federici, J. Linke, A. Loarte, J. Roth and K. Sato, Plasma facing and high heat flux materials – needs for ITER and beyond, (2002), https://doi.org/10.1016/S0022-3115(02)01175-3.

[2] L. K. Mansur, A. F. Rowcliffe, R. K. Nanstad, S. J. Zinkle, W. R. Corwin and R. E. Stoller, Materials needs for fusion, Generation IV fission reactors and spallation neutron sources – similarities and differences, (2004), https://doi.org/10.1016/j.jnucmat.2004.04.016.

[3] B. Cantor, Multicomponent and High Entropy Alloys, (2014); https://doi.org/10.3390/e16094749.

[4] B. Cantor, I. Chang, P. Knight and A. Vincent, Microstructural development in equiatomic multicomponent alloys, Mater. Sci. Eng. A 375–377, (2004); https://doi.org/10.1016/j.msea.2003.10.257.

[5] J. W. Yeh, S. K. Chen, S. J. Lin, J. Y. Gan, T. S. Chin, T. T. Shun, C. H. Tsau and S. Y. Chang, Nanostructured high-entropy alloys with multiple principal elements: novel alloy design, Advanced Engineering Materials, (2004), https://doi.org/10.1002/adem.200300567.

[6] J.-W. Yeh, Recent Progress in High-Entropy Alloys, European Journal of Control, (2006); https://doi.org/10.3166/acsm.31.633-648.

[7] A. Kirnbauer, A. Kretschmer, C. Koller, T. Wojcik, V. Paneta, M. Hans, J. Schneider, P. Polcik and P. Mayrhofer, Mechanical properties and thermal stability of reactively sputtered multi-principal-metal Hf-Ta-Ti-V-Zr nitrides, Surface and Coatings Technology, Volume 389, (2020); https://doi.org/10.1016/j.surfcoat.2020.125674.

[8] O. El Atwani, H. T. Vo, M. A. Tunes, C. Lee, A. Alvarado, N. Krienke, J. D. Poplawsky, A. A. Kohnert, J. Gigax, W. -Y. Chen, M. Li, Y. Q. Wang, J. S. Wrobel, D. Niguyen-Mahn, J. K. S. Baldwin, O. U. Tukac, E. Aydogan, S. Fensin and E. Martinez, A quinary WTaCrVHf nanocrystalline refractory high-entropy alloy withholding extreme irradiation environments, (2022), https://doi.org/10.1038/s41467-023-38000-y.

[9] M. A. Tunes, S. Fritze, B. Osinger, P. Willenshofer, A. M. Alvardo, E. Martinez, A. S. Menon, P. Ström, G. Greaves, E. Lewin, U. Jansson, S. Pogatscher, T. A. Saleh, V. M. Vishnyakov and O. El-Atwani, From high-entropy alloys to high-entropy ceramics: The radiation-resistant highly concentrated refractory carbide (CrNbTaTiW)C, (2023), https://doi.org/10.1016/j.actamat.2023.118856.

[10] Y. Zhang, M. A. Tunes, M. L. Crespillo, F. Zhang, W. L. Boldman, P. D. Rack, L. Jiang, C. Xu, G. Greaves and S. E. Donnelly, Thermal stability and irradiation response of nanocrystalline CoCrCuFeNi high-entropy alloy, (2019), https://doi.org/10.1088/1361-6528/ab1605.

[11] F. A. Garner, M. B. Toloczko and B. H. Sencer, Comparison of swelling and irradiation creep behavior of fcc-austenitic and bcc-ferritic/martensitic alloys at high neutron exposure, (2000), https://doi.org/10.1016/S0022-3115(99)00225-1.

[12] K. Nordlund, F. Djurabekova and G. Hobler, Large fraction of crystal directions leads to ion channeling, (2016), https://doi.org/10.1103/PhysRevB.94.214109.

[13] O. El-Atwani, J. A. Hinks, G. Greaves, J. P. Allain and S. A. Maloy, Grain size threshold for enhanced irradiation resistance in nanocrystalline and ultrafine tungsten, (2016), https://doi.org/10.1080/21663831.2017.1292326.

[14] J. H. Evans , The role of implanted gas and lateral stress in blister formation mechanisms, (1978), https://doi.org/10.1016/0022-3115(78)90145-9.

[15] F. I. Allen, P. Hosemann and M. Balooch, Key mechanistic features of swelling and blistering of helium-ion-irradiated tungsten, (2020), https://doi.org/10.1016/j.scriptamat.2019.11.039.

[16] A. Kretschmer, A. Kirnbauer, E. Pitthan, D. Primetzhofer, K. Yalamanchili, H. Rudigier and P. Mayrhofer, High-entropy alloy inspired development of compositionally complex superhard (Hf,Ta,Ti,V,Zr)-B-N coatings, (2022), https://doi.org/10.1016/j.matdes.2022.110695.

[17] A. Kirnbauer, A. Wagner, V. Moraes, D. Primetzhofer, M. Hans, J. Schneider, P. Polcik and P. H. Mayrhofer, Thermal stability and mechanical properties of sputtered (Hf,Ta,V,W,Zr)-diborides, Acta Mater. 200, (2020) 559–569. https://doi.org/10.1016/j.actamat.2020.09.018.

[18] J. P. Ziegler and J. P. Biersack, “SRIM - The Stopping and Range of Ions in Solids”, (1985), available online: http://www.srim.org/SRIM/SRIMINTRO.htm (accessed Jan. 16. 2024).

[19] Gwyddion, http://gwyddion.net, accessed 17 May 2024.

[20] P. S. Phani and W. C. Oliver, A critical assessment of the effect of indentation spacing on the measurement of hardness and modulus using instrumented indentation testing, (2019), https://doi.org/10.1016/j.matdes.2018.107563.

[21] ISO, For ISO Standard 14577-1 2002 Metallic Materials—Instrumented Indentation Test for Hardness and Materials Parameters—Part 1: Test Method., (2020), available online: https://www.iso.org/standard/56626.html (accessed Jan. 16. 2024).

[22] P. Hosemann, D. Kiener, Y. Wang and S. A. Maloy, Issues to consider using nano indentation on shallow ion beam irradiated materials, (2011), https://doi.org/10.1016/j.jnucmat.2011.11.070.

[23] A. K. Saxena, S. Brinckmann, B. Völker, G. Dehm and C. Kirchlechner, Experimental conditions affecting the measured fracture toughness at the microscale: Notch geometry and crack extension measurement, (2020), https://doi.org/10.1016/j.matdes.2020.108582.

[24] K. Matoy, H. Schönherr, T. Detzel, T. Schöberl, R. Pippan, C. Motz and G. Dehm, A comparative micro-cantilever study of the mechanical behavior of silicon based passivation films, (2009), https://doi.org/10.1016/j.tsf.2009.07.143.

[25] P. Sigmund, Theory of Sputtering. I. Sputtering Yield of Amorphous and Polycrystalline Targets, American Physical Society, (1969), https://doi.org/10.1103/PhysRev.184.383.

[26] M. Nakada, N. Ohshima and M. Okada, Crystal Orientation and Surface Roughness of Bi Films Prepared in Ionized Cluster Beam Apparatus, (1996), https://doi.org/10.1143/JJAP.35.714.

[27] Y. Yang, D. Frazer, M. Balooch and P. Hosemann, Irradiation damage investigation of helium implanted polycrystalline copper, (2018), https://doi.org/10.1016/j.jnucmat.2018.09.022.

[28] G. Lu, G. Q. Lu and Z. M. Xiao, Mechanical Properties of Porous Materials, (1999), https://doi.org/10.1023/A:1009669730778.

[29] M. D. Uchic and D. M. Dimiduk, A methodology to investigate size scale effects in crystalline plasticity using uniaxial compression testing, (2005), https://doi.org/10.1016/j.msea.2005.03.082.